JACS
JOURNAL OF THE AMERICAN CHEMICAL SOCIETY
Article
pubs.acs.org/JACS

Design and Properties of Intermediate-Sized Narrow Band-Gap Conjugated Molecules Relevant to Solution-Processed Organic Solar Cells

Xiaofeng Liu,*[,†,‡] Yanming Sun,[†,§] Ben B. Y. Hsu,[†,§] Andreas Lorbach,[†,‡,#] Li Qi,[†,‡] Alan J. Heeger,[†,§] and Guillermo C. Bazan*[,†,‡,⊥]

[†]Center for Polymers and Organic Solids, [‡]Department of Chemistry and Biochemistry, and [§]Department of Physics, University of California, Santa Barbara, California 93106, United States

[⊥]Center of Excellence for Advanced Materials Research (CEAMR), King Abdulaziz University, Jeddah, Saudi Arabia

Supporting Information

ABSTRACT: Increases in the molecular length of narrow band gap conjugated chromophores reveal potentially beneficial optical and electronic properties, thermal stabilities, and high power conversion efficiencies when integrated into optoelectronic devices, such as bulk heterojunction organic solar cells. With the objective of providing useful information for understanding the transition from small-sized molecules to polymers, as well as providing a general chemical design platform for extracting relationships between molecular structure and bulk properties, we set out to vary the electron affinity of the molecular backbone. Therefore, a series of donor (D)−acceptor (A) alternating narrow band gap conjugated chromophores were synthesized based on the general molecular frameworks: D^1-A^1-D^2-A^2-D^2-A^1-D^1 and D^1-A^1-D^2-A^2-D^2-A^2-D^2-A^1-D^1. When the central electron-accepting moiety (A^2) was varied or modified, two classes of molecules could be compared. First, we showed that the alteration of one single electron-accepting group, while maintaining the shape of the molecular framework, can effectively impact the optical properties and energy levels of the molecules. DFT ground state structure optimizations show similar "U" shape conformations among these molecules. Second, we examined how the site-specific introduction of fluorine atom(s) modifies the thermal properties in the solid state, while maintaining relatively similar optical and electrochemical features of interest. Structure−property relationship of such molecular systems could be rationally evaluated in the aspects of thermal-responsive molecular organizations in the solid state and dipole moments both in the ground and excited states. The impact of molecular structure on charge carrier mobilities in field effect transistors and the performance of photovoltaic devices were also studied.

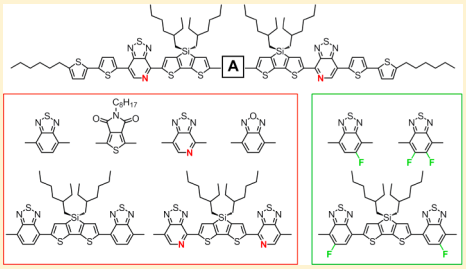

INTRODUCTION

Organic conjugated materials have been actively studied and integrated in semiconducting devices, including solar cells, light-emitting diodes, and field-effect transistors.[1−7] Thin film fabrication from such materials may involve thermal deposition or solution processing methods, and offer versatile techniques that could favor a large variety of substances.[8−12] Optical, electronic, and thermophysical properties, as well as the solid state organization, are particularly relevant for understanding overall device performance.[13−16] Design and synthetic strategies have been put forward to tailor molecular orbital energy levels and optical transitions, thus affording the opportunity to tailor materials properties toward specific device functions.[1,17−21] In particular, conjugated materials have received sustained interest for their utilization as electron-donating active components in organic photovoltaic (OPV) devices when blended with fullerene derivatives as electron acceptors to form the so-called "bulk heterojunction" (BHJ) structure.[22−25] To fulfill their function in efficient photon-current conversion, OPV materials should combine an overlap of their absorption bands with the solar spectrum with appropriate orbital energies and charge carrier mobilities.[26−32]

Light harvesting for OPV function requires materials to have a high absorption coefficient and an optical band gap (E_g) of 1.2−1.6 eV.[17,19] An effective and well-studied synthetic strategy to achieve such properties is to incorporate molecular electron donor (D) and acceptor (A) units in an alternating and conjugated manner.[33−36] The resulting push−pull nature along the molecular skeleton facilitates an intramolecular charge transfer and electronically delocalized structure.[37,38] Desired molecular orbital energy levels and E_g can thus be tuned through incorporation of a number of building blocks by a variety of different synthetic approaches.[39−43] Much of the related research has been focused on the use of macromolecules comprising an "infinite" number of D−A repeating units, i.e., "polymer" (Figure 1).[1,44−46] Advantages of polymeric materials include their high absorption coefficients, wide range of light absorption, and efficient charge carrier mobilities.[3,47,48] More-

Received: January 3, 2014
Published: March 24, 2014

   dx.doi.org/10.1021/ja413144u | J. Am. Chem. Soc. 2014, 136, 5697−5708

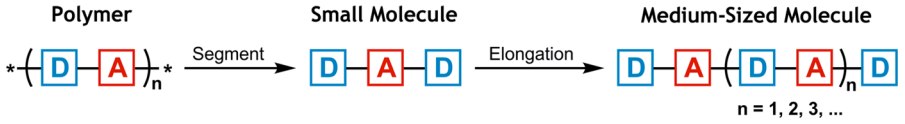

Figure 1. Cartoon depiction showing the structure transition from polymer to small molecule and back to medium-sized molecular systems, based on the D−A alternating characteristics.

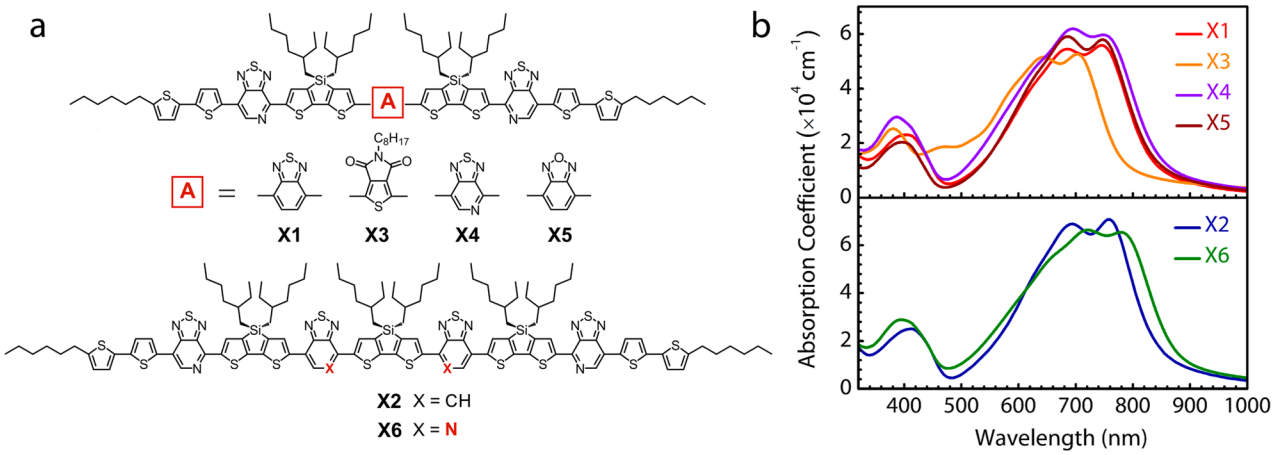

Figure 2. (a) The chemical structures of medium-sized molecules with various electron-accepting units, denoted as A and (b) UV−vis absorption spectra of the corresponding molecules in the solid states.

over, polymers are also well suited in terms of film quality and thermal robustness; considerations that have argued in favor of device stability.[49−51]

Research on D−A "small molecule" (Figure 1), analogues of polymer segments, is more recent.[52−58] As compared with their polymeric counterparts, small-sized molecular systems offer well-defined chemical structures. Instead of the conventional thermal deposition method, recent literature highlights the potential of solution processability for molecular systems.[53,57,59−61] Although not frequently discussed in detail, poorer film quality is frequently observed, relative to polymers, and remains a persistent challenge for device fabrication. Nevertheless, high solubility can be easily achieved with small-sized molecules and it allows a variety of basic organic transformations and purification techniques, such as regio-specific coupling and chromatography.[62,63] Rational molecular design based on the D−A concept has given rise to a large number of high performance building blocks with close-to-ideal material properties toward OPVs.[63−71]

A relevant structure for the design of molecular donors can be generally expressed as D^1-A-D^2-A-D^1, where D^1 and D^2 indicate different types of electron-rich aromatic subunits, i.e., 5′-hexyl-2,2′-bithiophene (BiTh) and dithieno(3,2-*b*;2′,3′-*d*)-silole (DTS), respectively. Molecules developed on the basis of this framework have found utilities in integration of BHJ solar cells with power conversion efficiencies (PCEs) comparable to the best value obtained with polymers.[72] Two of the examples have employed either a pyridal[2,1,3]thiadiazole (PT) or a 5-fluorobenzo[*c*][1,2,5]thiadiazole (f-BT) as acceptor A.[62,63] In the course of the synthesis, the incorporation of such heterocycles with asymmetric electronic structures can be used to achieve regioselectivity in palladium-catalyzed coupling reactions, promoting well-controlled chemical structures and high-yield production.[62,63]

Given that polymeric and molecular donor materials have their own advantages and drawbacks, it is useful to consider extracting the most relevant properties from both classes. Recently, we introduced well-defined molecular structures with continuous elongation of D−A characteristics, namely, "medium-sized molecules" (Figure 1).[69] Relative to their structurally related small-sized molecules, these materials exhibit effectively narrower E_g, while providing at the same time thermally more stable phases in the solid states. The larger molecular size also led to a desirable BHJ organization without processing additives and post thermal treatment, which considerably simplifies the process of solar cell device fabrication.

Realizing that medium-sized molecules may be able to combine some of the most desirable properties from both small molecules (e.g., well-defined crystallinity) and polymers (e.g., thermal stability and film quality), we set out to systematically design and synthesize a series of molecules based on the molecular skeletons of D^1-A^1-D^2-A^2-D^2-A^1-D^1 and D^1-A^1-D^2-A^2-D^2-A^2-D^2-A^1-D^1 (for specific structures see Figures 2a and 3a). We focus our studies on evaluating how structural variations influence bulk properties of interest in two aspects: (1) variation of the electron affinities of the A^2 subunit to control the molecular energy levels, optical and thermal properties, and (2) selective anchoring of fluorine atoms to the molecular frameworks to achieve favored electronic structures relevant to OPVs and enhanced thermal resistance in the bulk. We show how the electrostatic dipole moments in the ground and first excited states of each molecule are influenced by the molecular structure and their relevance to the bulk organization. We also examined how variations of the A^2 segment influence solid-state order upon heating. Finally, we evaluate the impact of acceptor unit A^2 on the charge carrier mobilities and photovoltaic properties. While the prediction of overall bulk behavior of organic semiconductors as a function of molecular connectivity remains an inexact science, the information herein provides a relevant step forward to

dx.doi.org/10.1021/ja413144u | *J. Am. Chem. Soc.* 2014, 136, 5697−5708

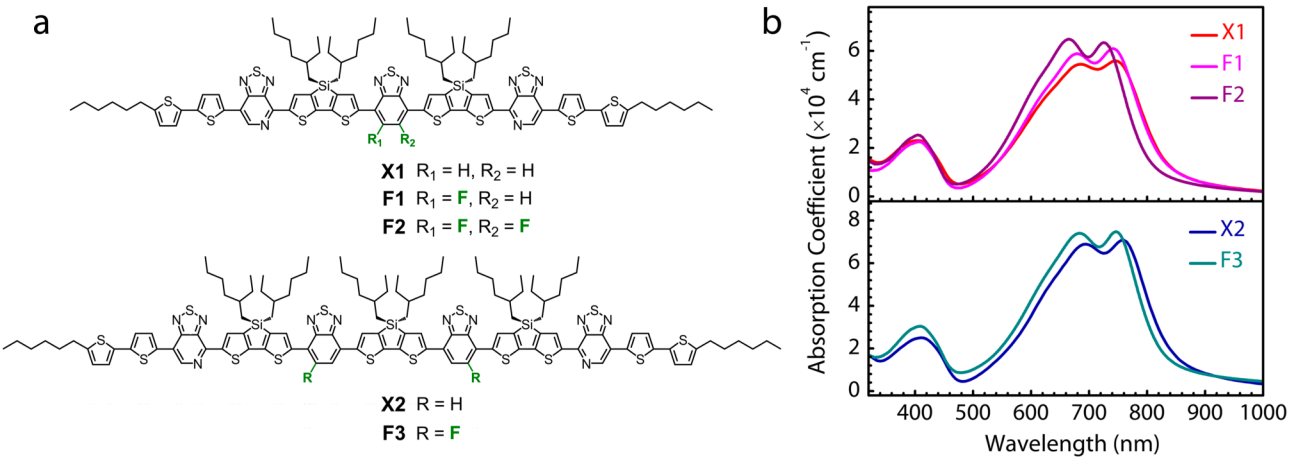

Figure 3. Chemical structures of molecular systems with site-specific fluorine substituents (a) and solid state UV−vis absorption spectra (b) of the corresponding medium-sized molecules. The structure of **X2** is depicted in a different way, compared to Figure 2, so to highlight its structural relationship to **F3**.

understanding the impact of specific functional groups when attached to a larger optical/electronic conjugated framework.

RESULTS AND DISCUSSION

Design and Synthesis of Molecular Systems. The nine molecules synthesized in this study can be assigned to two groups according to their molecular dimensions, as shown in Figures 2a and 3a. The first group, including **X1**, **X3**, **X4**, **X5**, **F1**, **F2**, has a general structure of D^1-A^1-D^2-A^2-D^2-A^1-D^1, where D^1, A^1, and D^2 represent BiTh, PT, and DTS, respectively, and A^2 varies among benzo[*c*][1,2,5]thiadiazole (BT) (**X1**), 5-octylthieno-[3,4-*c*]pyrrole-4,6-dione (TPD) (**X3**), PT (**X4**), benzo[*c*][1,2,5]oxadiazole (BO) (**X5**), f-BT (**F1**), and 5,6-difluorobenzo[*c*][1,2,5]thiadiazole (ff-BT) (**F2**). The other group combines larger molecules of the type D^1-A^1-D^2-A^2-D^2-A^2-D^2-A^1-D^1, in which D^1 (BiTh), A^1 (PT), and D^2 (DTS) remain unchanged, while the A^2 unit is altered among BT (**X2**), PT (**X6**), and f-BT (**F3**). These compounds provide well-defined, monodisperse chemical structures that, in contrast to polymers, allow unambiguous evaluation of molecular structure−property relationships. All molecules were built up via a series of Stille cross-coupling reactions between a previously reported monostannylated molecular building block and corresponding dibrominated counterparts.[69] Detailed reaction procedures and characterizations of all the compounds can be found in the Supporting Information. The preparation of a key intermediate (**3**, Scheme 1), was achieved by coupling

Scheme 1. Synthetic Entry into Intermediate 3

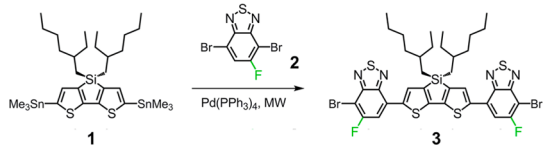

1 with 5-fluoro-4,7-dibromobenzo[*c*][1,2,5]thiadiazole (**2**) in the presence of $Pd(PPh_3)_4$ at 90 °C, with a recovered yield of 65%. Under these conditions, the bromo substituent in *meta* position to the fluorine atom is more reactive than the *ortho*-Br.[73] The regiochemistry of the resulting compound was determined by ^1H−^1H NOE NMR spectroscopy (Figure S1). Structures of all final molecules were confirmed through ^1H, ^{13}C, ^{19}F NMR spectroscopies, and field-desorption time-of-flight (FD-TOF) mass spectrometry (Figures S2 and S3). It is worth noting that the regioselectivity of the reaction is completely lost when higher temperatures or microwave-assisted heating are applied. In contrast to that, regioselective coupling to the brominated PT unit can be achieved under these conditions.[62] All nine molecules show excellent solubilities (>50 mg/mL) in chloroform at room temperature, owing to the multiple branched alkyl side chains. Shorter molecules **X3**, **X4**, **X5**, **F1**, and **F2** exhibited up to triply charged cationic species in FD-TOF mass spectra (same as **X1**), while longer molecules **X6** and **F3** gave additional quadruply charged species (same as **X2**).[69] It appears from this set of data that it is a reasonable and persistent trend that more extended molecular systems can stabilize more charges through more extensive electron delocalization.

Variation of Electron-Accepting Subunits. We first evaluate the role of a single electron-accepting group (shown as A in Figure 2a) by switching between moieties with different electron affinities within shorter molecules, i.e., **X1**, **X3**, **X4**, **X5**, and longer ones, i.e., **X2**, **X6**. Optical absorption spectra of the six molecules in dilute chloroform solution are shown in Figure S4, and the most relevant data are summarized in Table 1. Note that **X1** and **X2** were picked as similar congeners for the comparison of shorter and longer molecular systems, respectively. Solutions of **X1**−**X6** show broad optical absorption with distinct peaks at both higher and lower energy regions, with solution extinction coefficients (ε) of the absorption maxima (λ_{max}) at around 1×10^5 $M^{-1}\cdot cm^{-1}$ for shorter molecules (**X1**, **X3**, **X4**, and **X5**) and $(1.2-1.5) \times 10^5$ $M^{-1}\cdot cm^{-1}$ for longer ones (**X2** and **X6**). These absorption features are commonly seen with D−A conjugated molecular systems,[35,62,70,74] and the ε values are comparable with typical PT-containing polymers.[75] The incorporation of A^2 units with increasing electron affinities (TPD < BT < BO < PT)[19,76] yield progressive shifts of the absorption onsets (λ_{onset}) toward lower energy region; that is, **X3** exhibits a blue-shift (30 nm) of λ_{onset} while **X4** shows a red-shift (22 nm) of λ_{onset}, as compared with **X1**. The exception is that **X5** gives a blue-shift of 7 nm in λ_{onset} but a red-shift of 8 nm in λ_{max} with respect to **X1**.

While the absorption in solution reflects variations at the molecular level, in the solid state, however, molecular packing plays an important role.[77,78] Thin films were therefore prepared

dx.doi.org/10.1021/ja413144u | J. Am. Chem. Soc. 2014, 136, 5697−5708

Table 1. Optical Characteristics of the Molecules in the Solid State Showing λ_{max}, λ_{onset}, E_g and Summary of HOMO, LUMO Energy Levels, E_g Determined by Cyclic Voltammetry, and Theoretical Calculations[a]

	solution absorption		film absorption			CV			DFT		
molecule	λ_{max} (nm)	λ_{onset} (nm)	λ_{max} (nm)	λ_{onset} (nm)	E_g^{opt} (eV)	E_{HOMO} (eV)	E_{LUMO} (eV)	E_g^{elec} (eV)	E_{HOMO} (eV)	E_{LUMO} (eV)	E_g^{calc} (eV)
X1	670	756	748	860	1.44	−5.17	−3.73	1.44	−4.95	−3.26	1.69
X2	672	765	758	880	1.41	−5.04	−3.71	1.33	−4.88	−3.24	1.64
X3	648	726	714	800	1.55	−5.29	−3.73	1.56	−5.05	−3.26	1.79
X4	690	778	751	885	1.40	−5.17	−3.74	1.43	−4.99	−3.35	1.64
X5	678	749	749	870	1.43	−5.15	−3.71	1.44	−5.02	−3.32	1.70
X6	715	806	781	915	1.36	−5.11	−3.79	1.32	−4.96	−3.40	1.56
F1	666	745	742	842	1.47	−5.20	−3.73	1.47	−4.98	−3.29	1.69
F2	660	733	726	827	1.50	−5.26	−3.75	1.51	−5.02	−3.28	1.74
F3	670	760	746	858	1.45	−5.08	−3.69	1.39	−4.95	−3.29	1.66

[a]Films were prepared by spin-coating chloroform solution (10 mg/mL) of each molecule onto glass slides at a spin speed of 1500 rpm. CV measurements were carried out in chloroform solution (ca. 2 mg/mL), with Fc/Fc^+ as an internal reference. DFT calculations were performed at the B3LYP/6-311G(d,p) level to optimize the ground state geometries of the molecules. λ_{max} refers to the lowest-energy absorption peak for each molecule. λ_{onset}: absorption onset. E_g^{opt}: optical band gap. E_{HOMO}: HOMO energy level. E_{LUMO}: LUMO energy level. E_g^{elec}: electrochemical band gap. E_{HOMO} and E_{LUMO} obtained by DFT calculation refer to the first occupied and unoccupied (virtual) Kohn−Sham orbital energies, respectively. E_g^{calc} was calculated from the energy difference between frontier orbitals.

by spin-coating chloroform solutions (10 mg/mL) of each compound atop glass substrates, and their absorption spectra are shown in Figure 2b. The absorption bands of **X1**−**X6** reveal red-shifts in λ_{onset} of 104, 115, 74, 107, 121, and 109 nm, respectively, relative to their solution spectra. The smallest change in λ_{onset} observed for **X3** is likely because of the additional octyl side chain on the TPD unit, which may obstruct interchromophore $\pi-\pi$ interactions. Interestingly, integration of PT units instead of BT leads to broadened absorption profiles for **X4** and **X6**, with respect to their structural analogues, **X1** and **X2**, respectively. Although the reason for the broader absorption range remains unclear, increases in the coverage of solar spectrum in the near-infrared (NIR) region are beneficial for efficient photon harvesting. Film absorption coefficients (α) between 5×10^4 and 7×10^4 cm^{-1} were observed for all six molecules, which reflect their strong light-absorbing capabilities. Optical band-gaps were estimated from the λ_{onset} of the film absorptions as 1.44 (**X1**), 1.41 (**X2**), 1.55 (**X3**), 1.40 (**X4**), 1.43 (**X5**), and 1.36 eV (**X6**). It is reasonable that the molecule containing the highest number of electronegative PT units (**X6**) shows the narrowest band gap.

The highest occupied molecular orbital (HOMO) and lowest unoccupied molecular orbital (LUMO) energy levels were estimated by cyclic voltammetry (CV, see Figure S5);[79] the data are summarized in Table 1. Owing to the greater solubility of these molecular materials, relative to polymeric counterparts, it is possible to estimate energy levels via solution-based CV measurements, which interrogate single molecule properties more accurately than thin film-based CV. It is interesting to point out that altering the central electron-accepting A unit gives rise to only modest changes to LUMO energy level (−3.71 to −3.79 eV), with **X6** affording the lowest value. These observations reflect how the LUMO energies are largely dominated by the most electron-withdrawing PT fragment. HOMO energy levels were determined from the onsets of the first oxidation waves, and the values are in the range between −5.04 (**X2**) and −5.29 eV (**X3**) (Table 1). Electrochemical HOMO−LUMO energy gaps calculated from the oxidation and reduction potentials are in agreement with those estimated from film absorption onsets. The same information was also examined by using density functional theory (DFT), employing the B3LYP functional and 6-311G(d,p) basis set based on the optimized ground state geometry for each molecule (Supporting Information),[38] with results listed in Table 1. One observes that the energy level values obtained with optical, electrochemical, and theoretical approaches follow the same trends. The offset of the DFT values can be attributed to the fact that the model describes a single molecule in the gas phase neglecting any intermolecular interactions.[38] On the basis of the electrochemical measurements and theoretical expectations, **X3** possesses the deepest HOMO energy level, and should thus be most likely to achieve higher open circuit voltage (V_{oc}) within an OPV device based on blends with fullerene derivatives. The narrower band gap and broader absorption profile of **X6** provide the opportunity to achieve larger short circuit current (J_{sc}).

Impact of Site-Specific Fluorine Substituents. Attachment of fluorine substituents is known to be a useful design element to tune the properties of conjugated materials and their function within device configurations.[80−83] It is difficult, however, to clearly map out the impact of this substitution when considering conjugated polymer backbones, because they intrinsically possess a statistical distribution of structures.[84] In this study, however, it is possible to delineate the impact of site-specific installation of fluorine atom(s) onto molecular backbones by comparing the properties of **F1**, **F2**, and **F3**, with those of **X1** and **X2**, respectively (Figure 3a).

A comparison of the solution UV−vis absorption profiles of **F1**, **F2**, and **F3** with respect to **X1** and **X2** is provided in Figure S4. The introduction of fluorine atom(s) in **F1** and **F2** does not bring noticeable changes to the ε values, except for a ca. 7% increase in ε for **F3** (1.6×10^5 $M^{-1}\cdot cm^{-1}$) over **X2** (1.5×10^5 $M^{-1}\cdot cm^{-1}$). The λ_{max} values of **F1** (666 nm) and **F2** (660 nm) are blue-shifted by 4 and 10 nm, respectively, as compared with **X1** (670 nm), together with a decrease in λ_{onset} of 11 and 23 nm. Additional vibronic features are shown for **F1**, **F2**, and **F3**, which are most likely attributed to the increase in molecular rigidity and planarity through the fluorine−sulfur (F···S) interactions between adjacent aromatic units, i.e., DTS and f-BT/ff-BT.[85−87] When transitioning from solution to the solid state, the fluorinated molecules exhibit similarly broadened absorption profiles, with low energy bands ranging from 500 to 900 nm (Figure 3b). The α values of **F1** (6.1×10^4 cm^{-1}) and **F2** (6.3×10^4 cm^{-1}) are slightly higher than those for **X1** (5.6

dx.doi.org/10.1021/ja413144u | J. Am. Chem. Soc. 2014, 136, 5697−5708

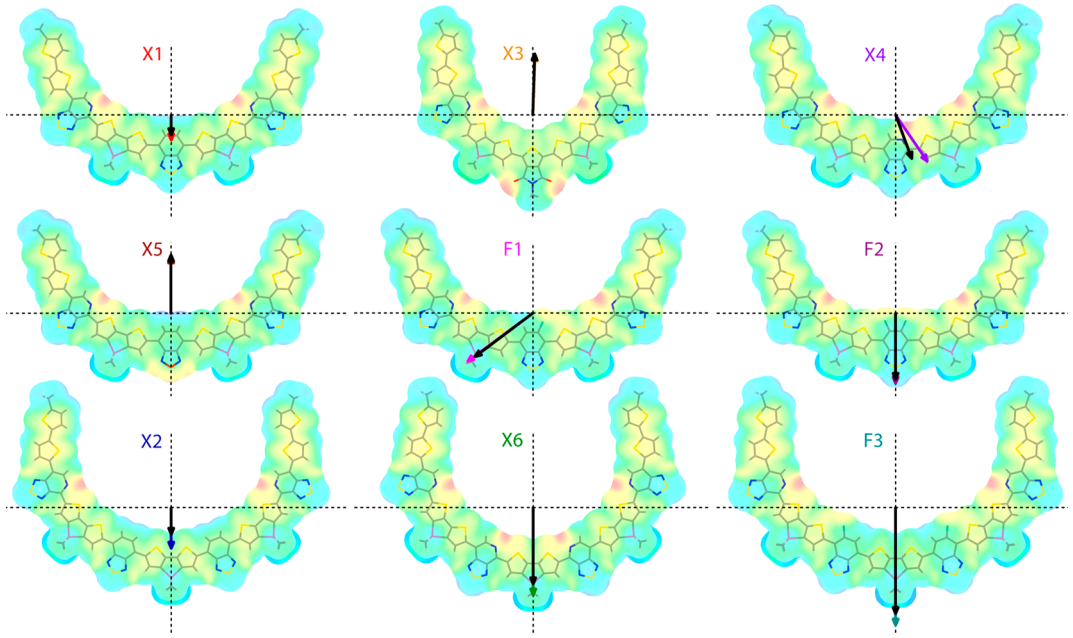

Figure 4. The lowest-energy conformations of the molecules **X1**−**X6** and **F1**−**F3** at ground states with surface mappings of electrostatic potentials in the range from −1 to +1 eV. Arrows indicate the magnitudes and directionalities of electrostatic dipole moments at the ground (black) and the first excited states (colored). Horizontal axis represents x direction, and vertical axis shows y direction.

$\times 10^4$ cm^{-1}). The same is true for **F3** (7.4×10^4 cm^{-1}) vs **X2** (7.1×10^4 cm^{-1}). In addition, one observes continuous blue-shifted λ_{onset} with increasing number of fluorine atoms on the central BT unit of **X1**, corresponding to optical band gaps of 1.47 eV (**F1**) and 1.50 eV (**F2**), vs 1.44 eV (**X1**). A longer molecular framework, i.e., two f-BT units instead of BTs (**F3** vs **X2**), leads to a 22 nm blue shift in λ_{onset}. It is worth pointing out that the increase in optical band gap observed for fluorinated molecules (**F1** and **F2** vs **X1**, **F3** vs **X2**) differs from reports from related polymer systems, where fluorination of the BT unit does not have an obvious impact on the absorption profiles.[80−82] One possibility is that the more disordered polymer structure blurs subtle influences by different chemical substituents on optical transitions.

As measured by CV and summarized in Table 1, the HOMO energy levels of **F1** (−5.20 eV) and **F2** (−5.26 eV) are only slightly deeper with respect to the nonfluorinated **X1** (−5.17 eV). The same is true for **F3** (−5.08 eV) vs **X2** (−5.04 eV). These observations indicate that within a relatively large molecular framework, the absolute HOMO energy levels correlate positively with the number of fluorine substituents on the central A^2 subunit, although the impact of this substitution is attenuated by virtue of the large molecular size. In contrast, changes in LUMO energy levels upon fluorine substitution are less pronounced (≤0.02 eV), which results in an increase of the band gap. From a broader perspective, these changes are not overly significant from a molecular optical properties viewpoint; however, as described in more detail below, we find that the C−H for C−F substitution leads to pronounced changes in the bulk thermal properties.

Ground State Conformational Preferences and Electrostatic Potentials in the Ground and First Excited States. Preferred molecular conformations and the influence of structure on the electrostatic distribution among the different molecules were probed via ab initio calculations on all molecules by using DFT at the B3LYP/6-311G(d,p) level of theory. The motivation behind these efforts stem from recent reports that correlate the effective molecular dipoles on the arrangements in the bulk and the crystallization tendencies as a function of molecular dipole.[88] Figure 4 shows relevant results from the DFT calculations. We note that the alkyl chains of all the molecules were truncated as methyl groups for more resource-effective calculations. To maximize computational efficiency, we first investigated the conformational freedom of each D−A fragment by employing relaxed potential energy surface scan and used these relaxed fragments (i.e., at their lowest-energy) to construct initial structure as input for DFT calculations (details can be found in the Supporting Information). The optimized "U"-shape ground state structures (previously described as "banana-like" for smaller systems) are in agreement with similar derivatives we have studied by means of single crystal X-ray diffraction.[89] We note here that energy differences between different conformations can be rather low (thermally accessible) and that it is therefore very likely that conformers other than the "U"-shaped ones also play an important role. However, we choose the most probable lowest energy conformation of each molecule for the following DFT studies. The general picture drawn here highlights how the asymmetry of the PT moiety plays an important role in favoring such "U" shape molecular geometry.

Mulliken atomic partial charges of each molecule were first analyzed with respect to their optimized lowest-energy geometries.[90] It is worth noting that the main structural features of these molecules involve the sp^2 hybridized pyridyl N atom (PT) and C−F functionality (f-BT/ff-BT). Good examples for each circumstance lie on the structurally asymmetric molecules, **X4** and **F1**, respectively, which allow a useful comparison of electronic structures between the two different halves of the same molecule. In particular, with respect to the central PT unit in **X4**, Mulliken atomic charge gives +0.328 e for the sulfur atom on the adjacent DTS that points toward the pyridyl N atom, which is more positive than the one pointing away (+0.312 e). The same is true for **F1**, where the Mulliken atomic charges were observed as +0.323 and +0.311 e,

dx.doi.org/10.1021/ja413144u | J. Am. Chem. Soc. 2014, 136, 5697−5708

for the corresponding sulfur atoms pointing toward and away from C−F substituent, respectively. Molecular electrostatic potential (ESP) mappings are shown in Figure 4, where red and blue colors show the most negative (−1 eV) and most positive (+1 eV) regions, respectively. One finds that the N atom from each PT subunit leads to a local maximum of negative ESP. Thus, it is reasonable that the sulfur atom from the DTS unit, which possesses a positive ESP, points to the most negative site, favoring the "U"-shape molecular conformation. Similar results were also observed for the C−F functionality. In combination with the study of Mulliken atomic charges, the results indicate ubiquitous N···S and/or F···S interactions across the series of molecules. Such interactions could provide, at least in part, a driving force for structural planarization, which in turn, facilitates $\pi-\pi$ stacking and allows for closer intermolecular contacts.

The calculations reveal that the notable variations of bending angles (θ) of the "U"-shaped molecular geometry are intrinsic to the changes of chemical structures. By assigning θ as the angle between the centroids of the central unit (**X1**, BT; **X3**, TPD; **X4**, PT; **X5**, BO; **F1**, f-BT; **F2**, ff-BT; for **X2**, **X6**, and **F3**, DTS) and the two endmost PT units, one determines θ = 129.3° for **X1**. With altering accepting unit from BT to TPD, PT, and BO, θ is found to be 107.7°(**X3**), 124.1° (**X4**), and 132.6° (**X5**). Besides the θ variation led by the different chemical structure (**X3**) and/or electron affinity (**X5**) of the A^2 unit, the 5° decrease in θ for **X4** relative to **X1** can be attributed to the extra N···S interaction brought by the central BT for PT substitution. **X6** (98.6°) similarly shows a 10° more acute value of θ compared to its BT-containing analogue, **X2** (108.4°). Surprisingly, as the number of F atoms increases, one observes a successive widening of θ for **F1** (131.1°) and **F2** (133.5°), relative to **X1**. A θ widening of 2.7° is also observed for **F3** (111.1°) vs **X2**. In terms of electrostatic interactions, the similar nature for F···S as compared to N···S does not lead to an expected θ sharpening, but the opposite is observed. One plausible reason may be that the larger size of C−F functionality over C−H or N increases the steric demands.

Excited state electronic structures were also calculated by employing time-dependent (TD) DFT with the same functional and basis set as the ground state calculation. The calculated electrostatic dipole moments for each molecule in the ground (μ_g) and excited (μ_e) states are summarized in Table 2, with the magnitude and directionality of the dipole vectors illustrated in Figure 4 (μ_g, black; μ_e, colored). Detailed calculation procedures, molecular orbital energy levels for the first excited state (Table S1), and dipole moment calculations (Table S2) can be found in Supporting Information. The high degree of planarity essentially cancels net dipole moments along the z direction (perpendicular to the conjugation plane) for all molecules. As shown by the black arrows in Figure 4, ground state dipole moments of the molecules point mostly toward the bottom of the "U" shape geometries (i.e., $-y$), and are calculated to be between 0.67 and 3.57 D in magnitude, except for **X3** and **X5**, in which both the electronegative pyrrole-dione and O atom from the BO unit lead to an inverted dipole direction (Figure 4). The asymmetric factors in **X4** and **F1** primarily dominate the direction and magnitude of the net dipole moments, leading to enlarged μ_{gx} (0.54 and 1.95 D in magnitudes, for **X4** and **F1**, respectively), while the rest of the molecules show dipole moments only along y-axis owing to their symmetry in the x direction.

Table 2. Summary of Calculated Dipole Moments for Molecules X1−X6 and F1−F3 at both the Ground and First Excited States[a]

molecule	μ_g (D)	μ_e (D)	$\Delta\mu_{ge}$ (D)
X1	0.67	0.85	0.18
X2	0.90	1.37	0.47
X3	2.06	2.04	0.02
X4	1.56	1.89	0.54
X5	1.96	1.90	0.06
X6	2.57	2.95	0.38
F1	2.44	2.74	0.30
F2	2.23	2.36	0.13
F3	3.57	3.96	0.39

[a] μ_g: ground state total dipole moment. μ_e: excited state total dipole moment. $\Delta\mu_{ge}$: dipole moment change from ground to excited state, calculated by following the equation described in the literature.[91]

Recent reports provide evidence that the dipole moment change in going from the ground to the first excited state ($\Delta\mu_{ge}$) influences the degree of photoinduced charge transfer within a molecule, and has an impact on the performance of OPV devices.[84,91] These studies suggest that the larger the $\Delta\mu_{ge}$, the lower the Coulombic binding energy of the excitons, thus facilitating intramolecular charge dissociation. It is thus relevant to begin understanding to what degree different combinations of electron-rich and electron-poor heterocycles can be brought together in order to tailor $\Delta\mu_{ge}$. Table 2 shows that the alteration of A^2 unit in **X1** framework among TPD and BO results in a decrease of $\Delta\mu_{ge}$. Larger variations of $\Delta\mu_{ge}$ were obtained for structurally asymmetric molecules (**X4** and **F1**), in comparison with the symmetric ones (**X1**, **X3**, **X5**, and **F2**), which further suggests the importance of examining the whole molecule instead of only a selected number of repeat units. Despite the asymmetric factor, a general decrease in $\Delta\mu_{ge}$ was shown for **F2** vs **X1**, and **F3** vs **X2**. These calculations provide relevant information for understanding the changes in charge distribution as a function of molecular structure and electronic state within a class of closely related structural analogues.

Thermal Response of Molecular Organization in the Solid State. Solid state thermal transitions were evaluated by using differential scanning calorimetry (DSC) under N_2 at a heating/cooling ramp of 10 °C/min. The results of this study are shown in Figure 5a, with heating cycles combined in the lower half and cooling cycles in the upper half. Table 3 summarizes relevant melting (T_m) and crystallization (T_c) temperatures, together with the enthalpies (ΔH_m and ΔH_c) associated with each process.

A useful comparison can be made using compounds **X1**, **X3**, **X4**, and **X5**, which only differ by the nature of the internal A unit. Changing BT (**X1**) for PT (**X4**) leads to negligible difference in T_m and a decrease in ΔH_m (~6 J/g). However, when the TPD core is introduced (**X3**), there is a more obvious decrease in both T_m and ΔH_m, together with cold crystallization behavior (134 °C), which is reasonably attributed to the presence of the flexible and nonpolar octyl group in TPD. Switching the internal unit to BO (**X5**) leads to the remarkable and unanticipated absence of any obvious transitions. Note that **X1** and **X5** are only different by virtue of a single isoelectronic S for O substitution out of 113 non-hydrogen atoms per molecule! It is at this stage worth mentioning that ease of crystallization is a practical typical requirement when

dx.doi.org/10.1021/ja413144u | J. Am. Chem. Soc. 2014, 136, 5697−5708

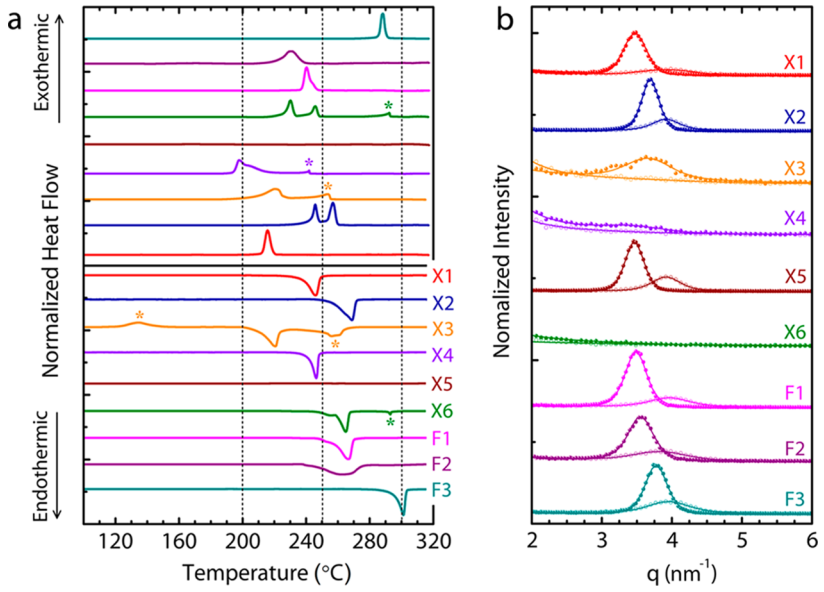

Figure 5. (a) DSC traces for molecules **X1**−**X6**, and **F1**−**F3**. Asterisks highlight weak peaks (cold crystallization for **X3** and liquid crystalline behavior for **X3**, **X4**, and **X6**). Dash lines indicate temperatures at 200, 250, and 300 °C. (b) Out-of-plane GIXRD profiles for all molecules before (open circles) and after (filled circles) thermal annealing at 170 °C for 60 s. Peak fitting for each curve is shown as solid line.

Table 3. Summary of Phase Transition Properties and GIXRD Parameters of the Molecules in the Solid State

	DSC				GIXRD			
	melting		crystallization		as-cast		annealed at 170 °C	
molecule	T_m (°C)	ΔH_m (J/g)	T_c (°C)	ΔH_c (J/g)	*d*-spacing (nm)	CCL (nm)	*d*-spacing (nm)	CCL (nm)
X1	246	26.0	216	24.8	1.6	7	1.8	18
X2	269	20.3	254, 244	19.2	1.6	13	1.7	22
X3	222	5.6	220	3.4	-	-	1.7	8
X4	246	20.5	198	20.2	-	-	1.8	7
X5	-	-	-	-	1.6	13	1.8	20
X6	265	15.8	246, 230	14.4	-	-	-	-
F1	267	28.6	239	28.5	1.6	9	1.8	17
F2	264	12.7	231	12.6	1.6	7	1.8	15
F3	301	19.2	288	18.9	1.6	9	1.7	17

considering donor molecules for BHJ solar cells, as this driving force aids in phase separation from the fullerene acceptors.

Similar to the structural relationship between **X1** and **X4**, the substitution of BT for PT in **X2**, i.e., **X6**, results in only a small drop in T_m (4 °C), while a larger T_c offset (14 °C) was observed. Out of all molecules, **X2** and **X6** stand out from the rest in that they exhibit strong exothermic transitions (**X2**, 254 °C; **X6**, 246 °C) ahead of crystallization, which may correspond to the presence of monotropic liquid crystalline phases.[69] Interestingly, liquid crystalline behavior was observed for molecules **X3** (257 °C) and **X6** (293 °C) during heating processes, and for **X3** (254 °C), **X4** (242 °C), and **X6** (292 °C) upon cooling, which hints that the incorporation of TPD or PT brings in driving forces for stabilizing mesophases.

Comparison of phase transitions from **F1**/**F2** vs **X1**, and **F3** vs **X2** reveals that fluorine substitution enhances thermal robustness. The DSC trace of **F1**, i.e., a mono fluorinated **X1**, shows an increase in both T_m and T_c of more than 20 °C. An additional fluorine substitution (i.e., **F2**) does not induce noticeable further increase in temperatures (3 and 8 °C lower in T_m and T_c, respectively, as compared to **F1**). Instead, broader melting and crystallization peaks emerge, along with relatively smaller enthalpies (Table 3), which indicate a weakening of crystallinity. Similarly, **F3** affords notable enhancements with respect to **X2** (32 °C in T_m and 44 °C in T_c). It is also worth noting that in contrast to the nonfluorinated analogues **X2** and **X6**, no semistable phases were observed for **F3**, suggesting that the melting and crystallization processes of **F3** are kinetically less hindered. Therefore, it is reasonable to conclude that C−H for C−F substitution on such discrete molecular frameworks likely induces an increase in intramolecular rigidity that facilitates organization in the solid state. Such information on melting and crystallization behaviors also has a practical relevance when it comes to exploring possible thermal annealing protocols that can improved the optoelectronic performance of thin films.

Internal bulk structures from each of these materials before and after thermal treatment at 170 °C for 1 min were examined by employing grazing incidence X-ray diffraction (GIXRD). Out-of-plane profiles with q values in the range of 2−6 nm^{-1} are shown in Figure 5b. Pristine films of each material were cast on (100) silicon substrates from chloroform solution (10 mg/mL). Curve fitting was carried out to determine the interlamellar *d*-spacing and crystallite correlation length (CCL) from each measurement, which were calculated based on peak maximum (q_{max}) and full width at half-maximum

dx.doi.org/10.1021/ja413144u | J. Am. Chem. Soc. 2014, 136, 5697−5708

(fwhm) as detailed in Supporting Information (Table S3). All as-cast films exhibit a *d*-spacing of 1.6 nm, except for films of **X3**, **X4**, and **X6**, in which no diffraction signals were detected, indicating that the lamellar ordering along the out-of-plane direction from these materials is not strongly present. It is surprising that **X5** shows a larger CCL (13 nm) than **X1** (7 nm), in contrast to the DSC measurement where **X5** shows no phase transitions. Thermal annealing of the films leads to an increase in *d*-spacing (0.1−0.2 nm), possibly due to relaxation of the solubilizing side chains, as well as sharpened scattering peaks and concomitant increase in CCL. Such features can be exemplified with the behavior of **X5**, for which thermal annealing leads to a CCL increase from 13 to 20 nm. Scattering signals of **X3** and **X4** films emerged after thermal treatment, with *d*-spacing measured as 1.7 and 1.8 nm, and CCLs of 8 and 7 nm, respectively. Regarding the effect of fluorine substitution (i.e., **F1**/**F2** vs **X1**, and **F3** vs **X2**), GIXRD of the as-cast films indicate differences in CCL (**F1**, 9 nm; **F2**, 7 nm; **X1**, 7 nm). Post-thermal treatment leads to a general increase in CCLs for **X1** (18 nm), **F1** (17 nm), and **F2** (15 nm), where the CCL of **F2** is now relatively lower. The most unexpected result is from the comparison of **X2** and **X6**, where **X2** exhibits distinct scattering signals both from as-cast (*d*-spacing = 1.6 nm, CCL = 13 nm) and annealed films (*d*-spacing = 1.7 nm, CCL = 22 nm). However, **X6** does not show any scattering within the *q* range of 2−6 nm^{-1} either before or after thermal treatment. In fact, a 2D wide-angle X-ray analysis (GIWAXS) indicates that **X6** adopts an exclusive "face-on" $\pi-\pi$ stacking orientation along the silicon surface normal (Figure S9). We currently cannot provide an explanation for the different molecular orientations observed for the two structural analogues (**X2** and **X6**).

Figure 6 shows the changes in percentile for film absorption coefficients, $(\alpha-\alpha_0)/\alpha_0$, versus wavelength for all nine

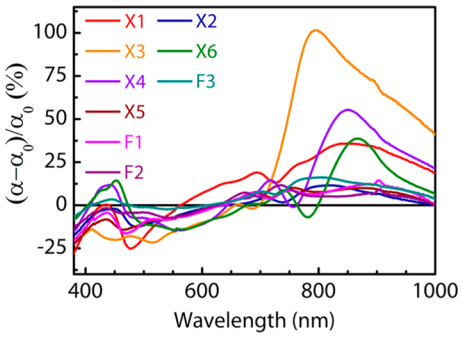

Figure 6. The percentile changes of solid state absorption coefficients along the visible-NIR region after thermal treatment of each film at 170 °C for 1 min with respect to as-cast condition. α and α_0 denote film absorption coefficients before and after thermal treatments, respectively.

molecules before and after thermal annealing at 170 °C for 1 min. All films were prepared on glass slides with conditions identical to the GIXRD experiments. Molecules **X3**, **X4**, and **X6** exhibit distinct changes beyond 800 nm: **X3** shows more than 100% increase in α at 795 nm, while **X4** (850 nm) and **X6** (866 nm) increase by 55% and 38%, respectively. Such significant thermal response is an indication of considerable bulk organization, which correlates well with GIXRD measurement where these three materials exhibit the most notable emergence of scattering peaks. Another important information is that minimum changes in absorption coefficients were revealed for molecules **F1**, **F2**, and **F3**, further corroborating the fact that more thermally robust bulk structures are obtained with appropriate fluorine substitution of the material.

Charge Carrier Mobilities. Charge transport properties were examined by using organic field-effect transistors (OFETs) with a top-contact and bottom-gated architecture. Thin films with thicknesses of ca. 30 nm were prepared by spin-coating 5 mg/mL of chloroform solution of each material atop heavily doped silicon wafer covered with 200 nm of thermally grown dielectric silicon dioxide, which were previously passivated with decyltrichlorosilane (Supporting Information). Devices were then thermally annealed for 10 min at various temperatures.

Figure 7a overviews the transfer curves of OFET devices fabricated from compounds **X1**−**X6** and **F1**−**F3** using as-cast conditions. Table 4 summarizes the hole mobility (μ_h), threshold voltage (V_{th}), and current on/off ratio (I_{on}/I_{off}) achieved for each device. All molecules present reasonable μ_h in the order of $10^{-1} \sim 10^{-3}$ $cm^2/(V\cdot s)$, a range that is useful for application in BHJ OPVs. Upon comparing **X3**, **X4**, and **X5** to **X1**, **X3** and **X4** show relatively lower μ_h, indicating less favored structural ordering was obtained by introducing either alkylated TPD or the asymmetric PT unit. In contrast, the **X5** device shows an as-cast mobility of 0.18 $cm^2/(V\cdot s)$, pointing toward a higher degree of structural ordering as compared to its analogues (**X1**, **X3**, and **X4**), in agreement with the largest CCL value determined from GIXRD. Similarly, structural variation in the case of **X2** versus **X6** further corroborates the essential role of electron deficient unit within molecular framework, where **X6** exhibits an μ_h (0.001 $cm^2/(V\cdot s)$) that is 1 order of magnitude lower than that of **X2** (0.04 $cm^2/(V\cdot s)$). However, differences in mobility have a complicated origin, which likely involves the different preference in molecular stacking orientation with respect to the substrates as observed for **X2** and **X6** (vide supra). The introduction of C−F functionality (i.e., **F1**, **F2**, and **F3**) does not bring obvious effect on their μ_h. In addition, thermal annealing experiments suggest that OFET devices based on all these molecules are thermally stable up to 200 °C (Table S4). Ambipolar charge transport behavior was observed for **X6**, with an electron mobility of 0.003 $cm^2/(V\cdot s)$, as shown in Figure 7b, which is interesting since this compound exhibits the lowest LUMO energy level among all molecules studied (Table 1).

Photovoltaic Characteristics. Photovoltaic properties of compounds **X1**−**X6** and **F1**−**F3** were evaluated in a BHJ configuration by incorporating (6,6)-phenyl-C_{61}-butyric acid methyl ester ($PC_{61}BM$) as an electron acceptor. All devices were operated under an N_2 atmosphere with the device architecture: indium tin oxide (ITO)/MoO_x/molecule:$PC_{61}BM$/Al. Active layers were prepared via spin-coating from chloroform solutions of molecule/$PC_{61}BM$ blends with a total solid concentration of 20 mg/mL. No solvent additives were included in the casting solution. The blend composition was adopted based on a previous study with **X1** and **X2**.[69] Active layers were treated by subjecting to thermal annealing (100 °C) before cathode deposition. Relevant photovoltaic parameters under AM 1.5G at 100 mA/cm^2 are detailed in Table 4. An interesting initial observation is that devices based on these materials operate well under a relatively low molecule/$PC_{61}BM$ weight ratio, as compared with lower molecular-weight counterparts.[67,88] This observation indicates that materials based on the medium-sized molecular framework

dx.doi.org/10.1021/ja413144u | J. Am. Chem. Soc. 2014, 136, 5697−5708

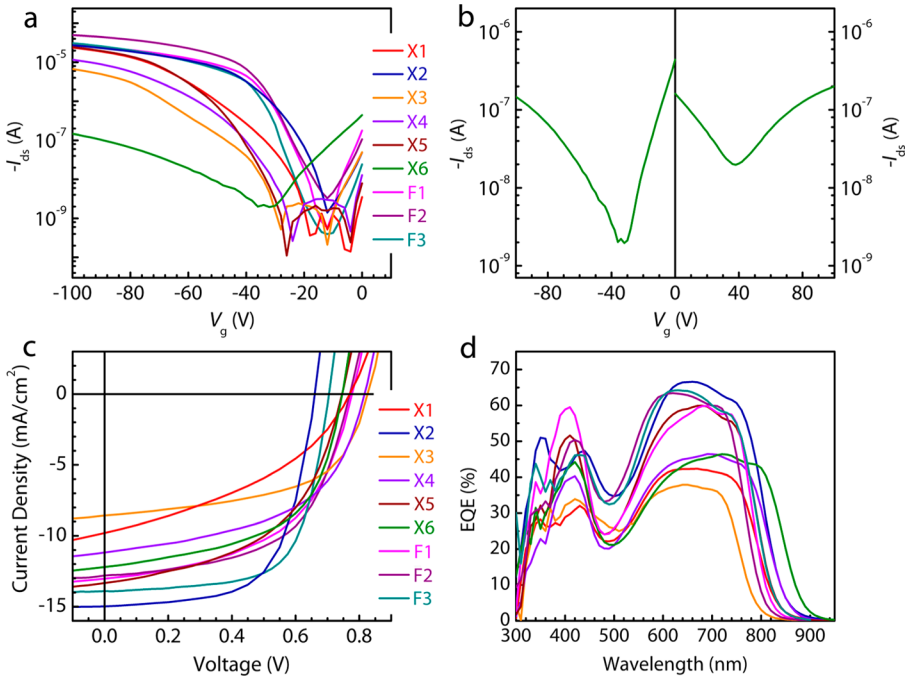

Figure 7. (a) Transfer characteristics of OFET devices built upon each molecule ahead of thermal treatment. (b) Ambipolar transfer behavior from **X6** device. (c) Current−voltage characteristics of molecule:$PC_{61}BM$ BHJ solar cell devices under as-cast condition. (d) EQE curves of the corresponding devices from (c).

Table 4. Summary of Field Effect Mobilities and Photovoltaic Parameters for Molecules X1−X6 and F1−F3

	OFET devices			OPV devices					
molecule	μ (cm^2/(V·s))	V_{Th} (V)	I_{on}/I_{off}	molecule:$PC_{60}BM$ (w/w)	thermal annealing	J_{sc} (mA/cm^2)	V_{oc} (V)	FF (%)	PCE (%)
X1	0.14	−30	10^4	60:40	w/o	9.8	0.77	39	3.0
					100 °C	13.6	0.71	60	5.8
X2	0.04	−10	10^4	50:50	w/o	15.0	0.66	64	6.3
					100 °C	15.2	0.66	64	6.4
X3	0.03	−40	10^3	60:40	w/o	8.6	0.83	56	4.0
					100 °C	4.0	0.83	50	1.7
X4	0.05	−30	10^4	60:40	w/o	11.2	0.82	52	4.8
					100 °C	12.6	0.75	61	5.7
X5	0.18	−35	10^4	60:40	w/o	13.3	0.75	51	5.1
					100 °C	12.7	0.72	60	5.5
X6	0.001 (h)[a]	−30 (h)	10^2 (h)	50:50	w/o	12.2	0.75	56	5.1
	0.003 (e)[b]	40 (e)	10^1 (e)		100 °C	12.6	0.75	62	5.8
F1	0.06	−18	10^4	60:40	w/o	13.0	0.78	53	5.3
					100 °C	12.9	0.75	65	6.3
F2	0.10	−20	10^4	60:40	w/o	12.8	0.77	57	5.6
					100 °C	13.5	0.76	59	6.1
F3	0.06	−20	10^5	50:50	w/o	13.9	0.71	67	6.5
					100 °C	14.2	0.71	65	6.5

[a]Hole mobility. [b]Electron mobility.

function best with a higher content of fullerene acceptors, which is often seen for conjugated polymers.[92−98]

Figure 7c,d details current density−voltage (J−V) characteristics and external quantum efficiencies (EQEs) for devices fabricated based on each molecule under as-cast conditions. Films cast from **X1** and **X3** afford devices with power conversion efficiency (PCE) of 3.0% and 4.0%, respectively, which are lower than those of their structural analogues **X4** (4.8%) and **X5** (5.1%). **X3** gives the highest V_{oc} (0.83 V), consistent with the deepest HOMO energy level. EQE spectra are consistent with optical absorption spectra of each material in the solid state. Thermal treatment on active layers prior to cathode deposition leads to enhanced PCEs for **X1** (5.8%), **X4** (5.7%), and **X5** (5.5%), and improvements in the fill factor (FF) in each case. The **X3** device, however, shows rather decreased PCE by ca. 50% of its original value, a result from a major loss in J_{sc} (4.0 vs 8.6 mA/cm^2). Interestingly, when subjecting to thermal treatment at elevated temperature, **X3** thin film exhibits the most sensitive response in optical absorption (Figure 6).

Comparison of molecules **F1**, **F2** vs **X1**, and **F3** vs **X2** allows one to obtain insight into the role of fluorine substitution: (1)

dx.doi.org/10.1021/ja413144u | J. Am. Chem. Soc. 2014, 136, 5697−5708

A successive improvement of PCE emerges for the as-cast devices of materials with increasing fluorination. Specifically, **F1** and **F2** devices show PCEs (FF) of 5.3% (53%) and 5.6% (57%), respectively, as compared to 3.0% (39%) obtained from **X1** device. Such improvement, especially in FF, suggests that fluorine substitution is able to drive the blend films toward a more favorable bulk organization during casting,[99] while the **X1**-containing film needs further treatment (e.g., thermal annealing) to achieve appropriate phase segregation. (2) Devices based on fluorinated molecules **F1** and **F2** exhibit suppressed sensitivity toward thermal treatment. For example, 100 °C-annealed **X1** device shows a major increase in PCE (~100%) over the as-cast device. In contrast, the same effects on **F1** (19%) or **F2** (9%) devices are considerably limited. It is obvious that, in case of **F1** and **F2**, better morphology for OPV function can be obtained immediately after casting. (3) Additional fluorine substitution on **X2** molecule (i.e., **F3**) does not provide further improvement in PCE (6.5%) under present conditions, mainly due to a composition of higher V_{oc} (0.71 V) and lower J_{sc} (13.9 mA/cm^2). Additionally, no changes in PCE upon thermal annealing can be observed, which is comparable to **X2**.

One highlight from this set of data is **X6**, a molecule containing four PT subunits, the OPV devices of which show EQE response beyond 900 nm, while at the same time a V_{oc} of 0.75 V. These values are relatively high for a molecular material with a band gap of 1.32 eV. The **X6**:$PC_{61}BM$ blend is able to achieve J_{sc} > 12 mA/cm^2 with a maximum EQE of 40%. Of particular note is that past studies indicated that materials with ambipolar charge transport seldom function well within OPV devices.[100] Surprisingly, the current study unveils a decent PCE (5.1%) obtained from **X6** devices without post treatment, which can be further improved to 5.8% by thermal treatment at 100 °C. Therefore, one can expect **X6** to be a promising candidate for OPV device optimization studies.

■ CONCLUSIONS

To establish a rational consideration of structurally novel medium-sized narrow band gap conjugated molecules toward high-efficiency and environmentally robust photovoltaic applications, we introduce herein the design, synthesis, and evaluation of nine structurally related chromophores with the following two D−A alternating architectures: D^1-A^1-D^2-A^2-D^2-A^1-D^1 and D^1-A^1-D^2-A^2-D^2-A^2-D^2-A^1-D^1. The main structural concerns with respect to material structure−property relationships include (1) comparison of molecular dimensionalities (molecular lengths), (2) variation of the central A^2 accepting unit, (3) selective fluorine substitution on BT subunit(s), and (4) incorporation of asymmetric building blocks (PT and f-BT). Such a modular structural data set allows one to identify design principles that can be applied to influence thermal resistance, self-organization, and ultimately charge carrier mobilities and optoelectronic properties.

By examining structural variations of the BiTh-PT-DTS-A^2-DTS-PT-BiTh theme, one finds that the A^2 subunit provides subtle changes in LUMO energy levels and a more obvious effect on HOMO energy levels. In the comparison between molecules **X1**, **X3**, **X4**, and **X5** with A^2 unit varying among BT, TPD, PT, and BO, respectively, **X3** shows the deepest HOMO energy level (−5.29 eV) and the widest band gap (1.56 eV), which correlates well with the higher V_{oc} (0.83 V) and lower J_{sc} (8.6 mA/cm^2) obtained in OPV devices. The results also disclose a great diversity in phase transitions and bulk organization within thin films. Specifically, materials with various A^2 units exhibit similar melting transition temperatures while differing greatly in terms of crystallization process and optical response to thermal treatment, in which **X5** shows much greater thermal resistance up to 170 °C than **X1**, **X3**, and **X4**. It is not obvious why no phase transitions (up to 320 °C) are observed by DSC for **X5**, even though XRD measurement reveals distinct scattering signals and notable solid state ordering. With the elongated molecular framework (BiTh-PT-DTS-A^2-DTS-A^2-DTS-PT-BiTh), **X6** (A^2, PT) has a narrower band gap than **X2** (A^2, BT), together with the deepest LUMO energy level (−3.79 eV) within the entire series of molecules. More interestingly, liquid crystalline behavior was observed for molecules **X3**, **X4**, and **X6**, suggesting structural factors that can contribute to stabilization of the molten phases and perhaps new approaches for processing of the materials. From a theoretical perspective, minor changes in chemical structures are also shown to notably alter molecular geometries, surface electrostatic potentials, and dipole moments both in the ground and the first excited state. Such changes are widely believed to influence molecular solid state organization, charge transport, exciton binding energy, and intramolecular charge separation upon photo irradiation.

Some unexpected yet intriguing results follow and are worth future investigation. (1) A preliminary observation shows that structural analogues **X2** and **X6** hold completely different preferences in molecular orientation (edge-on vs face-on) in the solid state, which may in turn lead to interesting anisotropic charge transport properties. (2) The role of fluorine substituents, which has been of interest previously in conjugated polymer analogues, can be more clearly identified in these well-defined molecules, as shown by the data in Tables 1−4.

Despite the great diversity in optical, thermal, and morphological properties, one finds the generality that all of the materials show charge carrier mobilities that are useful for photovoltaic applications (i.e., $10^{-1} \sim 10^{-3}$ cm^2/(V·s)). Consequently, solar cell devices based on these materials show PCEs in the range of 4.0−6.5% without significant optimization, which confirms that these medium-sized molecular frameworks are generally competitive alternatives for polymeric OPV materials. Of interest is that fluorine substituents provide nearly optimal performance directly from solutions that lack solvent additives; thermal annealing improvements are not significant. One therefore starts to observe the emergence of functional chemical groups that can be used to gain control over the kinetically confined evolution of the BHJ morphology. It is also worth emphasizing that the ambipolar material **X6** shows an encouraging performance in a conventional OPV device (PCE = 5.8%).

As a closing note, we realize that most of typical small molecular (and polymeric) donor materials require delicate morphology control to achieve solar cell devices with higher efficiency. It is thus important to emphasize that these medium-sized molecules demonstrate competitive solar cell performances (>5%) with simple device architecture in the absence of processing additives and postdeposition treatments, which reinforces the significance of molecular design principles toward the medium-sized conjugated molecules as the next generation of OPV donor materials. Whether the upfront investment in synthetic complexity is offset by simplicity in device fabrication remains an open question.

■ ASSOCIATED CONTENT

Supporting Information

Detailed experimental procedures, synthesis and characterization of all molecules, FD-TOF mass spectra, solution absorption spectra, CV, DFT and TD-DFT calculations, X-ray measurements, OFET and OPV device preparation and testing. This material is available free of charge via the Internet at http://pubs.acs.org.

■ AUTHOR INFORMATION

Corresponding Authors

xliu@chem.ucsb.edu
bazan@chem.ucsb.edu

Present Address

[#]Institut für Anorganische Chemie, Julius-Maximilians-Universität Würzburg, Am Hubland, 97074 Würzburg, Germany.

Notes

The authors declare no competing financial interest.

■ ACKNOWLEDGMENTS

Financial support of this study was provided by the Office of Naval Research (N00014-11-1-0284) for the synthesis of molecules, National Science Foundation (DMR 0856060), and Department of Energy, Office of Basic Energy Sciences under award number DE-FG02-08ER46535 for device testing. We acknowledge support from the Center for Scientific Computing from the CNSI, MRL: an NSF MRSEC (DMR-1121053) and NSF CNS-0960316. A.L. wishes to thank the Alexander von Humboldt Foundation for a Feodor Lynen Research Fellowship for postdoctoral researchers. The authors also thank Dr. Obum Kwon for providing dibrominated BT and TPD building blocks, Louis A. Perez for 2D GIWAXS measurement and insightful discussion on GIXRD experiment and data analysis, and Shu-Hua Chou for helpful discussion on DFT calculation and result interpretation.

■ REFERENCES

(1) Cheng, Y.-J.; Yang, S.-H.; Hsu, C.-S. *Chem. Rev.* **2009**, *109*, 5868−5923.
(2) Segura, J. L.; Martín, N.; Guldi, D. M. *Chem. Soc. Rev.* **2005**, *34*, 31−47.
(3) Günes, S.; Neugebauer, H.; Sariciftci, N. S. *Chem. Rev.* **2007**, *107*, 1324−1338.
(4) Burroughes, J. H.; Bradley, D. D. C.; Brown, A. R.; Marks, R. N.; Mackay, K.; Friend, R. H.; Burns, P. L.; Holmes, A. B. *Nature* **1990**, *347*, 539−541.
(5) Lo, S.-C.; Burn, P. L. *Chem. Rev.* **2007**, *107*, 1097−1116.
(6) Allard, S.; Forster, M.; Souharce, B.; Thiem, H.; Scherf, U. *Angew. Chem., Int. Ed.* **2008**, *47*, 4070−4098.
(7) Facchetti, A. *Chem. Mater.* **2011**, *23*, 733−758.
(8) Chen, J.; Cao, Y. *Acc. Chem. Res.* **2009**, *42*, 1709−1718.
(9) Moulé, A. J.; Meerholz, K. *Adv. Funct. Mater.* **2009**, *19*, 3028−3036.
(10) Peet, J.; Heeger, A. J.; Bazan, G. C. *Acc. Chem. Res.* **2009**, *42*, 1700−1708.
(11) Zakhidov, A. A.; Lee, J.-K.; DeFranco, J. A.; Fong, H. H.; Taylor, P. G.; Chatzichristidi, M.; Ober, C. K.; Malliaras, G. G. *Chem. Sci.* **2011**, *2*, 1178−1182.
(12) O'Neill, M.; Kelly, S. M. *Adv. Mater.* **2011**, *23*, 566−584.
(13) Dang, M. T.; Hirsch, L.; Wantz, G.; Wuest, J. D. *Chem. Rev.* **2013**, *113*, 3734−3765.
(14) Jo, S. B.; Lee, W. H.; Qiu, L.; Cho, K. *J. Mater. Chem.* **2012**, *22*, 4244−4260.
(15) Wen, Y.; Liu, Y.; Guo, Y.; Yu, G.; Hu, W. *Chem. Rev.* **2011**, *111*, 3358−3406.
(16) Chen, J.-T.; Hsu, C.-S. *Polym. Chem.* **2011**, *2*, 2707−2722.
(17) Zhou, H.; Yang, L.; You, W. *Macromolecules* **2012**, *45*, 607−632.
(18) Son, H. J.; Carsten, B.; Jung, I. H.; Yu, L. *Energy Environ. Sci.* **2012**, *5*, 8158−8170.
(19) Li, Y. *Acc. Chem. Res.* **2012**, *45*, 723−733.
(20) Henson, Z. B.; Müllen, K.; Bazan, G. C. *Nat. Chem.* **2012**, *4*, 699−704.
(21) Beaujuge, P. M.; Fréchet, J. M. J. *J. Am. Chem. Soc.* **2011**, *133*, 20009−20029.
(22) Peumans, P.; Uchida, S.; Forrest, S. R. *Nature* **2003**, *425*, 158−162.
(23) Koetse, M. M.; Sweelssen, J.; Hoekerd, K. T.; Schoo, H. F. M.; Veenstra, S. C.; Kroon, J. M.; Yang, X.; Loos, J. *Appl. Phys. Lett.* **2006**, *88*, 083504.
(24) Cates, N. C.; Gysel, R.; Beiley, Z.; Miller, C. E.; Toney, M. F.; Heeney, M.; McCulloch, I.; McGehee, M. D. *Nano Lett.* **2009**, *9*, 4153−4157.
(25) Roncali, J. *Acc. Chem. Res.* **2009**, *42*, 1719−1730.
(26) Scharber, M. C.; Mühlbacher, D.; Koppe, M.; Denk, P.; Waldauf, C.; Heeger, A. J.; Brabec, C. J. *Adv. Mater.* **2006**, *18*, 789−794.
(27) Bilby, D.; Kim, B. G.; Kim, J. *Pure Appl. Chem.* **2011**, *83*, 127−139.
(28) O'Boyle, N. M.; Campbell, C. M.; Hutchison, G. R. *J. Phys. Chem. C* **2011**, *115*, 16200−16210.
(29) Duan, C.; Huang, F.; Cao, Y. *J. Mater. Chem.* **2012**, *22*, 10416−10434.
(30) Kirkpatrick, J.; Nielsen, C. B.; Zhang, W.; Bronstein, H.; Ashraf, R. S.; Heeney, M.; McCulloch, I. *Adv. Energy Mater.* **2012**, *2*, 260−265.
(31) Zhang, L.; Pei, K.; Zhao, H.; Wu, S.; Wang, Y.; Gao, J. *Chem. Phys. Lett.* **2012**, *543*, 199−204.
(32) Walker, B.; Liu, J.; Kim, C.; Welch, G. C.; Park, J. K.; Lin, J.; Zalar, P.; Proctor, C. M.; Seo, J. H.; Bazan, G. C.; Nguyen, T.-Q. *Energy Environ. Sci.* **2013**, *6*, 952−962.
(33) Chang, Y.-T.; Hsu, S.-L.; Chen, G.-Y.; Su, M.-H.; Singh, T. A.; Diau, E. W.-G.; Wei, K.-H. *Adv. Funct. Mater.* **2008**, *18*, 2356−2365.
(34) Öktem, G.; Balan, A.; Baran, D.; Toppare, L. *Chem. Commun.* **2011**, *47*, 3933−3935.
(35) Wang, M.; Hu, X.; Liu, P.; Li, W.; Gong, X.; Huang, F.; Cao, Y. *J. Am. Chem. Soc.* **2011**, *133*, 9638−9641.
(36) Biniek, L.; Schroeder, B. C.; Nielsen, C. B.; McCulloch, I. *J. Mater. Chem.* **2012**, *22*, 14803−14813.
(37) Pron, A.; Gawrys, P.; Zagorska, M.; Djurado, D.; Demadrille, R. *Chem. Soc. Rev.* **2010**, *39*, 2577−2632.
(38) Risko, C.; McGehee, M. D.; Brédas, J.-L. *Chem. Sci.* **2011**, *2*, 1200−1218.
(39) Mercier, L. G.; Leclerc, M. *Acc. Chem. Res.* **2013**, *46*, 1597−1605.
(40) Carsten, B.; He, F.; Son, H. J.; Xu, T.; Yu, L. *Chem. Rev.* **2011**, *111*, 1493−1528.
(41) Bannock, J. H.; Krishnadasan, S. H.; Nightingale, A. M.; Yau, C. P.; Khaw, K.; Burkitt, D.; Halls, J. J. M.; Heeney, M.; de Mello, J. C. *Adv. Funct. Mater.* **2013**, *23*, 2123−2129.
(42) Zhang, X.; Tian, H.; Liu, Q.; Wang, L.; Geng, Y.; Wang, F. *J. Org. Chem.* **2006**, *71*, 4332−4335.
(43) Yokoyama, A.; Suzuki, H.; Kubota, Y.; Ohuchi, K.; Higashimura, H.; Yokozawa, T. *J. Am. Chem. Soc.* **2007**, *129*, 7236−7237.
(44) Brabec, C. J.; Gowrisanker, S.; Halls, J. J. M.; Laird, D.; Jia, S.; Williams, S. P. *Adv. Mater.* **2010**, *22*, 3839−3856.
(45) Li, J.; Grimsdale, A. C. *Chem. Soc. Rev.* **2010**, *39*, 2399−2410.
(46) Po, R.; Maggini, M.; Camaioni, N. *J. Phys. Chem. C* **2010**, *114*, 695−706.
(47) Subramaniyan, S.; Kim, F. S.; Ren, G.; Li, H.; Jenekhe, S. A. *Macromolecules* **2012**, *45*, 9029−9037.
(48) Tsao, H. N.; Cho, D. M.; Park, I.; Hansen, M. R.; Mavrinskiy, A.; Yoon, D. Y.; Graf, R.; Pisula, W.; Spiess, H. W.; Müllen, K. *J. Am. Chem. Soc.* **2011**, *133*, 2605−2612.

(49) Ma, W.; Yang, C.; Gong, X.; Lee, K.; Heeger, A. J. *Adv. Funct. Mater.* **2005**, *15*, 1617−1622.
(50) Cho, S.; Seo, J. H.; Park, S. H.; Beaupré, S.; Leclerc, M.; Heeger, A. J. *Adv. Mater.* **2010**, *22*, 1253−1257.
(51) Ong, K.-H.; Lim, S.-L.; Tan, H.-S.; Wong, H.-K.; Li, J.; Ma, Z.; Moh, L. C. H.; Lim, S.-H.; de Mello, J. C.; Chen, Z.-K. *Adv. Mater.* **2011**, *23*, 1409−1413.
(52) Velusamy, M.; Huang, J.-H.; Hsu, Y.-C.; Chou, H.-H.; Ho, K.-C.; Wu, P.-L.; Chang, W.-H.; Lin, J. T.; Chu, C.-W. *Org. Lett.* **2009**, *11*, 4898−4901.
(53) Li, Y.; Guo, Q.; Li, Z.; Pei, J.; Tian, W. *Energy Environ. Sci.* **2010**, *3*, 1427−1436.
(54) Mikroyannidis, J. A.; Sharma, S. S.; Vijay, Y. K.; Sharma, G. D. *ACS Appl. Mater. Interfaces* **2010**, *2*, 270−278.
(55) Sharma, G. D.; Suresh, P.; Mikroyannidis, J. A.; Stylianakis, M. M. *J. Mater. Chem.* **2010**, *20*, 561−567.
(56) Steinberger, S.; Mishra, A.; Reinold, E.; Levichkov, J.; Uhrich, C.; Pfeiffer, M.; Bäuerle, P. *Chem. Commun.* **2011**, *47*, 1982−1984.
(57) Lin, Y.; Ma, L.; Li, Y.; Liu, Y.; Zhu, D.; Zhan, X. *Adv. Energy Mater.* **2013**, *3*, 1166−1170.
(58) Ye, D.; Li, X.; Yan, L.; Zhang, W.; Hu, Z.; Liang, Y.; Fang, J.; Wong, W.-Y.; Wang, X. *J. Mater. Chem. A* **2013**, *1*, 7622−7629.
(59) Huang, J.; Zhan, C.; Zhang, X.; Zhao, Y.; Lu, Z.; Jia, H.; Jiang, B.; Ye, J.; Zhang, S.; Tang, A.; Liu, Y.; Pei, Q.; Yao, J. *ACS Appl. Mater. Interfaces* **2013**, *5*, 2033−2039.
(60) Li, Z.; He, G.; Wan, X.; Liu, Y.; Zhou, J.; Long, G.; Zuo, Y.; Zhang, M.; Chen, Y. *Adv. Energy Mater.* **2012**, *2*, 74−77.
(61) Walker, B.; Kim, C.; Nguyen, T.-Q. *Chem. Mater.* **2011**, *23*, 470−482.
(62) Welch, G. C.; Perez, L. A.; Hoven, C. V.; Zhang, Y.; Dang, X.-D.; Sharenko, A.; Toney, M. F.; Kramer, E. J.; Nguyen, T.-Q.; Bazan, G. C. *J. Mater. Chem.* **2011**, *21*, 12700−12709.
(63) van der Poll, T. S.; Love, J. A.; Nguyen, T.-Q.; Bazan, G. C. *Adv. Mater.* **2012**, *24*, 3646−3649.
(64) Lee, O. P.; Yiu, A. T.; Beaujuge, P. M.; Woo, C. H.; Holcombe, T. W.; Millstone, J. E.; Douglas, J. D.; Chen, M. S.; Fréchet, J. M. J. *Adv. Mater.* **2011**, *23*, 5359−5363.
(65) Loser, S.; Bruns, C. J.; Miyauchi, H.; Ortiz, R. P.; Facchetti, A.; Stupp, S. I.; Marks, T. J. *J. Am. Chem. Soc.* **2011**, *133*, 8142−8145.
(66) Shang, H.; Fan, H.; Liu, Y.; Hu, W.; Li, Y.; Zhan, X. *Adv. Mater.* **2011**, *23*, 1554−1557.
(67) Sun, Y.; Welch, G. C.; Leong, W. L.; Takacs, C. J.; Bazan, G. C.; Heeger, A. J. *Nat. Mater.* **2012**, *11*, 44−48.
(68) Mishra, A.; Bäuerle, P. *Angew. Chem., Int. Ed.* **2012**, *51*, 2020−2067.
(69) Liu, X.; Sun, Y.; Perez, L. A.; Wen, W.; Toney, M. F.; Heeger, A. J.; Bazan, G. C. *J. Am. Chem. Soc.* **2012**, *134*, 20609−20612.
(70) Henson, Z. B.; Welch, G. C.; van der Poll, T.; Bazan, G. C. *J. Am. Chem. Soc.* **2012**, *134*, 3766−3779.
(71) Zhou, J.; Wan, X.; Liu, Y.; Zuo, Y.; Li, Z.; He, G.; Long, G.; Ni, W.; Li, C.; Su, X.; Chen, Y. *J. Am. Chem. Soc.* **2012**, *134*, 16345−16351.
(72) Kyaw, A. K. K.; Wang, D. H.; Wynands, D.; Zhang, J.; Nguyen, T.-Q.; Bazan, G. C.; Heeger, A. J. *Nano Lett.* **2013**, *13*, 3796−3801.
(73) Sharif, M.; Zeeshan, M.; Reimann, S.; Villinger, A.; Langer, P. *Tetrahedron Lett.* **2010**, *51*, 2810−2812.
(74) Mazzio, K. A.; Yuan, M.; Okamoto, K.; Luscombe, C. K. *ACS Appl. Mater. Interfaces* **2011**, *3*, 271−278.
(75) Ying, L.; Hsu, B. B. Y.; Zhan, H.; Welch, G. C.; Zalar, P.; Perez, L. A.; Kramer, E. J.; Nguyen, T.-Q.; Heeger, A. J.; Wong, W.-Y.; Bazan, G. C. *J. Am. Chem. Soc.* **2011**, *133*, 18538−18541.
(76) Blouin, N.; Michaud, A.; Gendron, D.; Wakim, S.; Blair, E.; Neagu-Plesu, R.; Belletete, M.; Durocher, G.; Tao, Y.; Leclerc, M. *J. Am. Chem. Soc.* **2008**, *130*, 732−742.
(77) Kim, J. *Pure Appl. Chem.* **2002**, *74*, 2031−2044.
(78) Würthner, F.; Kaiser, T. E.; Saha-Möller, C. R. *Angew. Chem., Int. Ed.* **2011**, *50*, 3376−3410.
(79) Cardona, C. M.; Li, W.; Kaifer, A. E.; Stockdale, D.; Bazan, G. C. *Adv. Mater.* **2011**, *23*, 2367−2371.
(80) Zhou, H.; Yang, L.; Stuart, A. C.; Price, S. C.; Liu, S.; You, W. *Angew. Chem., Int. Ed.* **2011**, *50*, 2995−2998.
(81) Price, S. C.; Stuart, A. C.; Yang, L.; Zhou, H.; You, W. *J. Am. Chem. Soc.* **2011**, *133*, 4625−4631.
(82) Zhang, Y.; Zou, J.; Cheuh, C.-C.; Yip, H.-L.; Jen, A. K.-Y. *Macromolecules* **2012**, *45*, 5427−5435.
(83) Bronstein, H.; Frost, J. M.; Hadipour, A.; Kim, Y.; Nielsen, C. B.; Ashraf, R. S.; Rand, B. P.; Watkins, S.; McCulloch, I. *Chem. Mater.* **2013**, *25*, 277−285.
(84) Stuart, A. C.; Tumbleston, J. R.; Zhou, H.; Li, W.; Liu, S.; Ade, H.; You, W. *J. Am. Chem. Soc.* **2013**, *135*, 1806−1815.
(85) Sakamoto, Y.; Komatsu, S.; Suzuki, T. *J. Am. Chem. Soc.* **2001**, *123*, 4643−4644.
(86) Osuna, R. M.; Ortiz, R. P.; Ruiz Delgado, M. C.; Sakamoto, Y.; Suzuki, T.; Hernández, V.; López Navarrete, J. T. *J. Phys. Chem. B* **2005**, *109*, 20737−20745.
(87) Raya, A.; Mora, M. A. *Polymer* **2004**, *45*, 6391−6397.
(88) Takacs, C. J.; Sun, Y.; Welch, G. C.; Perez, L. A.; Liu, X.; Wen, W.; Bazan, G. C.; Heeger, A. J. *J. Am. Chem. Soc.* **2012**, *134*, 16597−16606.
(89) Welch, G. C; Bakus, R. C., II; Teat, S. J.; Bazan, G. C. *J. Am. Chem. Soc.* **2013**, *135*, 2298−2305.
(90) Mulliken, R. S. *J. Chem. Phys.* **1955**, *23*, 1833.
(91) Carsten, B.; Szarko, J. M.; Son, H. J.; Wang, W.; Lu, L.; He, F.; Rolczynski, B. S.; Lou, S. J.; Chen, L. X.; Yu, L. *J. Am. Chem. Soc.* **2011**, *133*, 20468−20475.
(92) Zhong, H.; Li, Z.; Deledalle, F.; Fregoso, E. C.; Shahid, M.; Fei, Z.; Nielsen, C. B.; Yaacobi-Gross, N.; Rossbauer, S.; Anthopoulos, T. D.; Durrant, J. R.; Heeney, M. *J. Am. Chem. Soc.* **2013**, *135*, 2040−2043.
(93) Park, S. H.; Roy, A.; Beaupré, S.; Cho, S.; Coates, N.; Moon, J. S.; Moses, D.; Leclerc, M.; Lee, K.; Heeger, A. J. *Nat. Photonics* **2009**, *3*, 297−303.
(94) Coffin, R. C.; Peet, J.; Rogers, J.; Bazan, G. C. *Nat. Chem.* **2009**, *1*, 657−661.
(95) Bronstein, H.; Chen, Z.; Ashraf, R. S.; Zhang, W.; Du, J.; Durrant, J. R.; Tuladhar, P. S.; Song, K.; Watkins, S. E.; Geerts, Y.; Wienk, M. M.; Janssen, R. A. J.; Anthopoulos, T.; Sirringhaus, H.; Heeney, M.; McCulloch, I. *J. Am. Chem. Soc.* **2011**, *133*, 3272−3275.
(96) Piliego, C.; Holcombe, T. W.; Douglas, J. D.; Woo, C. H.; Beaujuge, P. M.; Fréchet, J. M. J. *J. Am. Chem. Soc.* **2010**, *132*, 7595−7597.
(97) Li, W.; Roelofs, W. S. C.; Wienk, M. M.; Janssen, R. A. J. *J. Am. Chem. Soc.* **2012**, *134*, 13787−13795.
(98) Dou, L.; Chen, C.-C.; Yoshimura, K.; Ohya, K.; Chang, W.-H.; Gao, J.; Liu, Y.; Richard, E.; Yang, Y. *Macromolecules* **2013**, *46*, 3384−3390.
(99) Tumbleston, J. R.; Stuart, A. C.; Gann, E.; You, W.; Ade, H. *Adv. Funct. Mater.* **2013**, *23*, 3463−3470.
(100) Bura, T.; Leclerc, N.; Fall, S.; Lévêque, P.; Heiser, T.; Retailleau, P.; Rihn, S.; Mirloup, A.; Ziessel, R. *J. Am. Chem. Soc.* **2012**, *134*, 17404−17407.